

## Research Article

# Investigation on True Stress-Strain Curves of Flat and Corner Regions of Cold-Formed Section Using 3D Digital Image Correlation Method

Bo Xu,<sup>1,2,3</sup> Junwu Xia ,<sup>1,2,3</sup> Renwei Ma,<sup>1,2,3</sup> Jian Wang,<sup>1,2</sup> Xiaomiao Chen,<sup>1,2,3</sup> Hongfei Chang ,<sup>1,2</sup> and Lihai Zhang<sup>4</sup>

<sup>1</sup>Jiangsu Key Laboratory of Environmental Impact and Structural Safety in Engineering, China University of Mining and Technology, Xuzhou 221116, China

<sup>2</sup>State Key Laboratory for Geomechanics and Deep Underground Engineering, China University of Mining and Technology, Xuzhou 221116, China

<sup>3</sup>Jiangsu Collaborative Innovation Center for Building Energy Saving and Construction Technology, Xuzhou 221116, China

<sup>4</sup>Department of Infrastructure Engineering, The University of Melbourne, Melbourne, Victoria 3010, Australia

Correspondence should be addressed to Junwu Xia; xiajunwu100@163.com

Received 11 June 2019; Revised 1 September 2019; Accepted 9 November 2019; Published 16 December 2019

Academic Editor: Emanuele Brunesi

Copyright © 2019 Bo Xu et al. This is an open access article distributed under the Creative Commons Attribution License, which permits unrestricted use, distribution, and reproduction in any medium, provided the original work is properly cited.

The true stress-strain curve is the critical method to describe the practical material mechanical performance and the essential precondition to develop the advanced numerical simulation. Experimental, analytical, and numerical procedures were performed in present research to investigate the true stress-strain curves of flat and corner regions of the cold-formed channel section. The coupon tests with the 3D digital image correlation system were conducted on flat and corner specimens to directly obtain the true stress-strain curves. The experimental results indicate that the tensile secondary-hardening phenomenon at the plastic strain stage was observed in the true stress-strain curves of flat coupons, and initial strain hardening behavior was produced in that of corner coupons. Flat region exhibits a significant improvement of true ultimate strength compared to the engineering value. The stress status of the corner region is developed to ultimate strength at the early strain phase and exhibits a slight increase compared with the nominal values at the plastic phase. Cold-rolling action limits the ductility performance of the corner region, which highly restrains the tensile strain hardening at the plastic condition. Thus, the true yielding strength of the corner region is obviously higher, but the true ultimate strength is significantly lower than that of the flat region. Together with the optical measuring results, a trilinear model with two-stage strain hardening and a simplified trilinear models were established for describing the true stress-strain curves of flat and corner regions, respectively. The load-displacement curves from numerical simulations fit very well with those of coupon tests, which validate the reliability of the optic measurement and the dependability of the simplified constitutive models.

## 1. Introduction

Cold-formed components, manufactured in factories by cold rolling or press-braking, are increasingly applied in steel structures due to superior strength and high stiffness-to-weight ratio [1–4]. As shown in Figure 1, various types of cold-formed sections such as square hollow section, channel section, and angle section are generally used in cold-formed steel structures [5–9]. During the cold-working process,

plastic deformation and strain hardening are generated in corner regions, which cause the significantly different material mechanical performance compared with the flat regions [10–13]. True stress-strain curve, presenting the relationship between true stress and strain, is the key method to describe the true metallic material performance at full stages [14–16]. Furthermore, the true material mechanical parameters make the great contribution to the accurate development of numerical simulation [17].

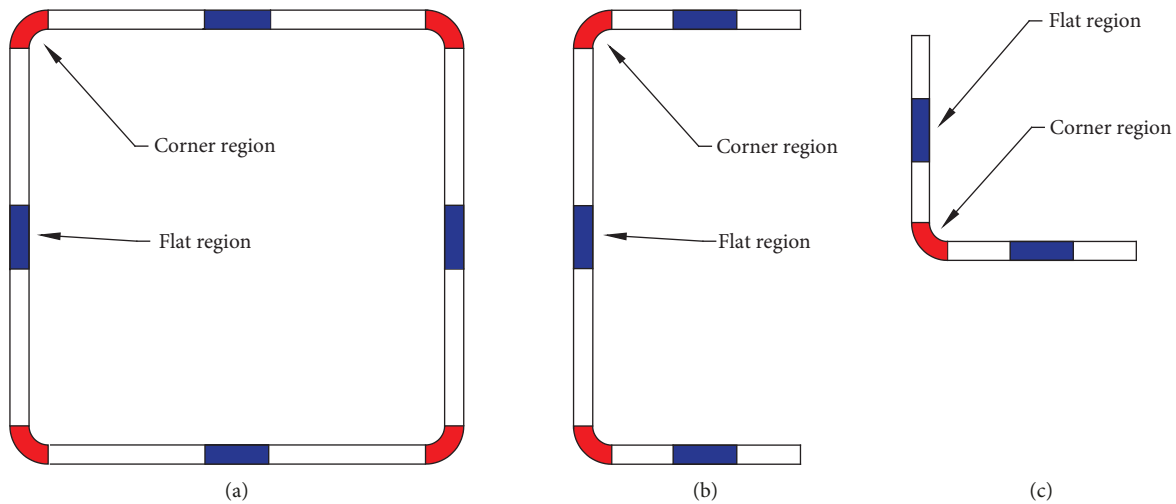


FIGURE 1: Cold-formed sections: (a) square hollow section; (b) steel channel section; (c) angle section.

It was found that the mechanical characteristics of flat and corner regions of cold-formed sections exhibit obvious mechanical nonuniformity [4, 9, 12]. Conventionally, the engineering stress-strain curves of coupons were investigated by several authors to describe the properties of flat and corner regions. Cabezas and Celentano characterized the material response of the sheet steel specimens using experimental-numerical methodology [18]. Li et al. carried out coupon tensile tests on the flat regions and corner regions, which captured the difference in failure modes and evaluated the effect of cold working on the improvement of yielding strength as well as the reduction of ductility [4, 18]. Afshan et al. conducted a large number of tensile tests on flat and corner coupons taken from square hollow sections (SHS), rectangular hollow sections (RHS), and circular hollow section (CHS), presenting engineering stress-strain curves and further obtaining constitutive model parameters [1, 2]. Based on the engineering stress-strain curves from coupon tests and the corresponding finite element analysis (FEA), it was captured that the material characteristics of the corner location in cold-formed sections were highly enhanced compared with those of the flat location due to cold working, while the stress value in engineering curves was defined directly by  $F/A_0$ , where  $F$  indicates the measured uniaxial force and  $A_0$  denotes the initial section area of coupons. This ignored the reduction of cross-section area during uniaxial tensile loading so that the increasingly obvious errors between the engineering and true stress were produced especially at the postnecking stage. It was therefore obtained that the engineering stress-strain curves could not accurately describe the practical full-stage constitutive relations.

Unlike to the engineering stress-strain curve, the true stress-strain curve, considering the decrease of section area, presents the practical material property. The key issue to determine the true stress-strain curve is to obtain the complete stress and strain tensor in the uniaxial test. Several attempts were conducted to indirectly obtain the true stress-strain curves from the coupon test results. Zhang et al. developed the numerical study on the diffuse necking behavior

of tensile specimens with rectangular cross section, which gained the cross-section area reduction and further determined the true stress-logarithmic strain relationship [19, 20]. Joun et al. presented a new numerical method by which the correlation between engineering and true stress-strain curve was established so that the true curves can be acquired [21, 22]. Bridgman performed a force-equilibrium type of analysis to include the effect of stress triaxiality in the neck on flow localization and applied a correction to the average true stress in order to obtain proper flow stress. These numerical procedures indirectly captured the true stress-strain curves, while certain assumptions and mediate convert in these studies would reduce the accuracy of results [23]. Actually, once the cross-section area of coupons was measured during loading, the true stress can be captured, and the true stress-strain curves thereby were determined accurately. Digital image correlation (DIC) technique with the advantage of full-field measurement was widely used in coupon tests on several bar specimens and flat specimens to directly measure the section area value. Li et al. applied the optic measuring method with the multicamera DIC system in dog-bone flat coupon test, by which the displacement and strain field were described intuitively and the true stress-strain curves of the metal sheet were captured [24]. Using the DIC, Paul et al. observed the three-dimensional deformation of rounded bar specimens during coupon tests and determined the true stress-strain curves [25, 26]. Coppieters et al. applied an inverse technique-based optical full-field measurement to identify the hardening behavior of thin sheets in the post-necking [27], which took into account the multiaxial stress and strain state. It was seen that the three-dimension DIC was the effective technique to acquire the true stress-strain curves of coupons. The true material properties of the round bar and sheet metal specimens have been fully evaluated with the 3D DIC technique while the true stress-strain curve of corner region coupons is widely produced in all sorts of cold-formed sections which is necessary to further investigate specifically.

In the present study, an optical measuring system based on 3D digital image correlation was proposed. In this way, the

true stress-strain curves corresponding to corner and flat regions of cold-formed profiles can be directly identified. Considering the mechanical nonuniformity of cross sections, the true stress-strain behaviours of corner and flat regions were individually determined, which could describe the accurate mechanical performance of cold-formed sections and evaluate the practical mechanical behaviours of cold-formed components. The coupon tests with the multicamera DIC system were conducted on the flat and corner specimens. By this way, the tensile failure modes, load-displacement curves, and true stress-strain curves were obtained. Furthermore, the trilinear model with two-stage strain hardening and simplified trilinear models of the true stress-strain curves were, respectively, established for the flat and corner regions in the cold-formed section based on the optic measurement results. Finally, the FE models of the flat and corner specimens assigned the simplified true constitutive models were developed for validating the DIC method and analytical results.

## 2. Experimental Programme

**2.1. Principle of Measurement with 3D Digital Image Correlation.** The three-dimensional full-field measurement system was established based on the working principles of binocular computer stereo vision and digital image correlation to describe the 3D displacement and strain field. Figure 2 shows the scheme of the 3D full-field measurement system. As shown in Figure 2(a), two industrial cameras were arranged in this innovate test system on the side of the observed specimens to continuously record the speckle images during the entire uniaxial loading process. As shown in Figure 2(b), numerous speckle photos were posttreated based on the principle of DIC. Every measurement image with the random speckle pattern can be divided into square image facets. Each of these facets represents its center point which was used similar to the ellipse center point of the reference point markers as the identification point. Based on these facet matchings, the displacement and strain fields of the observed area can be obtained. Using GOM software, a facet size of 19 pixels and a subset size of 361 were set to calculate the 3D displacement field ( $u, v, w$ ) of coupons, and the Green-Lagrange strain ( $\epsilon'$ ) was thereby obtained in the DIC measuring system by the gauge length ( $D_0$ ) and the corresponding displacement ( $D$ ) as shown in equation (1). The key point to achieve the true stress-strain curve was to capture the true section area of coupons in tests. For the flat specimens with a rectangular cross section, the section width and its reduction were straightly measured. As the isotropic metal material, the transverse strain of steel sheet specimens was measured directly and then defined as the strain in the thickness direction so that the variation of flat thickness was captured. Furthermore, the true cross-section area ( $A_t$ ) was gained during the test and the true stress ( $\sigma_t$ ) can be obtained by equation (2). As for the corner coupons with a 90° circle cross section, the outer ring arc length can be directly measured. Similar to the principle of achieving the true thickness of a flat coupon, the tangential strain on the outer surface of corner specimens was measured so that the thickness reduction and true thickness were further

obtained. Therefore, the true cross-section area and true stress-strain curve can be determined in the following way:

$$\epsilon' = \frac{D}{D_0} + \frac{1}{2} \left( \frac{D}{D_0} \right)^2, \quad (1)$$

$$\sigma_t = \frac{F}{A_t}. \quad (2)$$

**2.2. Flat and Corner Coupons.** In the series of coupon tests, six standard dog-bone flat specimens and six corner specimens were extracted from the flat and corner locations of a cold-formed channel component made of Q235 steel as shown in Figure 3(a). The details and dimensions of flat coupons with cross section 15 mm × 6 mm were designed according to the GB/T 228.1-2010 standard [28] as shown in Figures 3(b) and 3(c). In cold-formed sections, the cold working mainly influenced the material properties of corner regions [1, 2]. Thus, the six corner coupons were taken from the curved portions as shown in Figure 3(d), and the corner coupons with a quarter circle cross section of 12 mm outside diameter and 6 mm wall thickness are demonstrated in Figure 3(e). The six flat coupons were divided into two groups and each group contained three specimens. These two groups of flat specimens were named as TW-1~TW-3 and BW-1~BW-3. Similarly, the six corner samples were divided two groups and, respectively, named as TB-1~TB-3 and BB-1~BB-3. The detailed naming method was defined as follows: “T” and “B,” respectively, represented the different extracting locations of the two groups of samples. According to the difference in cutting regions between flat and corner specimens in cold-formed channel sections, “W” and “B” individually the web flat and bending corner locations. In addition, “1~3” denoted the three specimens in each group. As shown in Figure 4, the random speckle pattern was sprayed on the surface of flat and corner specimens prior to tensile tests as the basis of image-related information.

**2.3. Test Setup.** Figure 5 shows the arrangement of the 3D DIC measurement system. As shown in Figure 5(a), a 50 kN tensile testing machine was used to complete the uniaxial coupon test at a speed of 1 mm/min in accordance with the GB/T 228.1-2010 standard [28]. A pair of parallel chucks were installed to clamp the flat specimens in uniaxial tensile tests. As to the corner specimens, a pair of chucks with a quarter circle ring notch were fixed up to clamp these specimens with nonrectangular and noncircular cross sections. On front of the coupons, the digital image correlation device with two industrial cameras and blue light LED was built to capture images at a frequency of 10 Hz. The solution of the two cameras was 2752 × 2000 pixels and the focus length was 50 mm. In addition, Figure 5(b) shows the diagram of optical measurement. The camera angle ( $\alpha$ ) was set to be 25°. The measuring distance ( $l_m$ ) was 600 mm and the based distance between two cameras ( $d_c$ ) was 270 mm. In particular, the ratio of speckle pixels and calibration distance was previously determined using a calibration plate, and the multicamera image device was started synchronously with

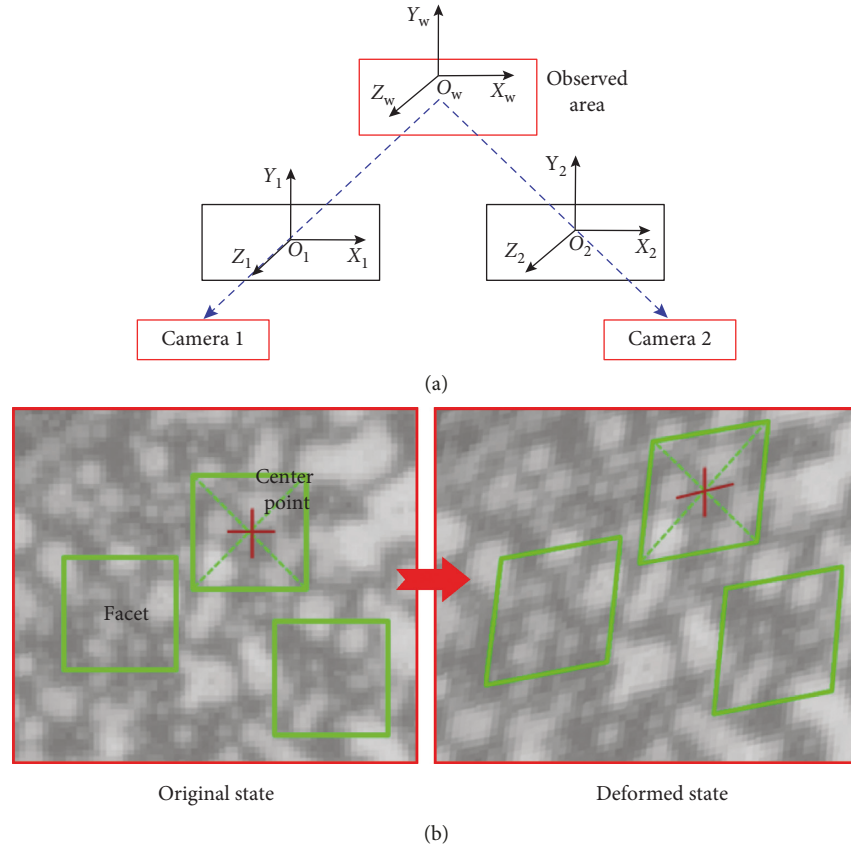


FIGURE 2: Scheme of the 3D full-field measurement system. (a) DIC measurement diagram; (b) DIC calculation diagram.

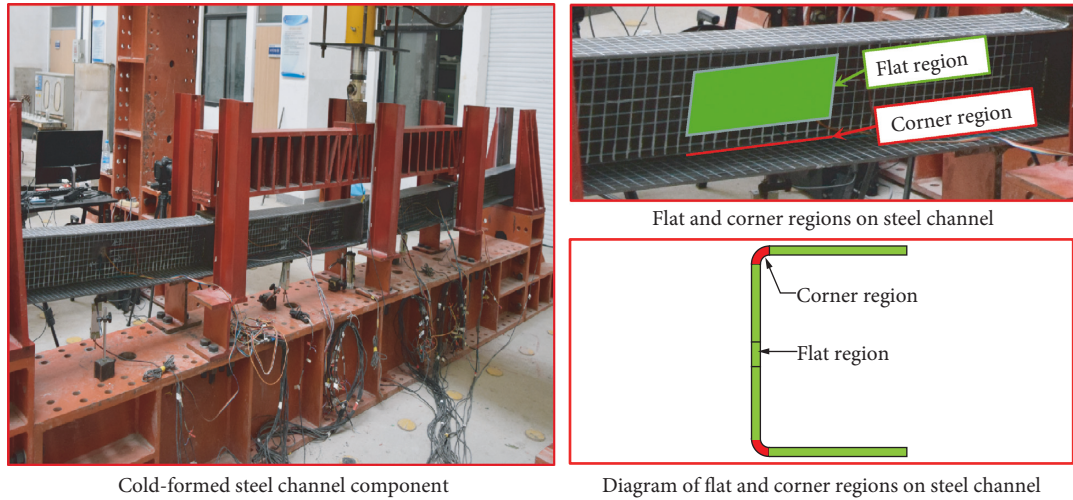
the tensile test machine in this 3D full-field measurement system so that the 3D displacement, strain matrix, and uniaxial force can be obtained directly during the whole loading process. Besides, with the noncontact optic analysis technique, the errors of extensometer and chuck slippage produced in conventional coupon test can be avoided in this test system, which leads to the superior measuring precision. By this way, the uniaxial force, true cross-section area, and strain value of flat and corner coupons during the whole loading process were captured; thus, the true stress-strain curves were obtained to evaluate the true material mechanical performance of flat and corner regions in the cold-formed section.

### 3. Experimental Result

**3.1. Failures and Load-Displacement Curves.** Coupon tests were conducted on the six flat specimens, namely, TW-1~TW-3 and BW-1~BW-3, and the six corner specimens, namely, TB-1~TB-3 and BB-1~BB-3, with the deformation and strain status continuously captured using the 3D DIC system. Figure 6(a) demonstrates the deformation and strain distributions of flat coupons under uniaxial displacement loading. It is shown that typical necking deformations occurred on the intermediate section locations of all flat specimens and the failures happened at the displacement value of about 24 mm. The deformation modes of all corner coupons were also continuously observed and failure

displacement values were about 7 mm. For parts of corner specimens, typical necking deformations were observed at the center of the specimens, but necking deformations at borders of parallel segments were produced in other specimens as shown in Figure 6(b). With the whole parallel area kept in the observed area in this DIC system, the full-field 3D displacement and strain information were recorded and postprocessed so that the displacement and strain values were obtained in this way. It was seen that the plastic deformation performance and ductility characteristics of the corner region in the cold-formed section were highly reduced compared with the flat region due to the cold working.

As shown in Figure 6, the longitudinal lengths of observed areas ( $D_c$ ) on flat and corner coupons increased gradually under the uniaxial loading, and length values were consistently measured. On this basis, the displacement of gauge lengths of tensile specimens was obtained by  $D = D_L - D_0$  in accordance with the GB/T 228.1-2010 standard [28], where  $D$ ,  $D_L$ , and  $D_0$  denote the real-time displacement, real-time gauge length, and initial gauge length, respectively, so that the engineering strain ( $\epsilon_n$ ) can be calculated by  $\epsilon_n = D/D_0$ . In addition, the loading values applied in these specimens were directly captured by the simultaneously triggered tensile test machine. Therefore, the load versus displacement curves of flat and corner coupons were determined as indicated in Figure 7. It is shown that the flat specimens with wall thickness of 6 mm exhibit the features of typical load-displacement of a

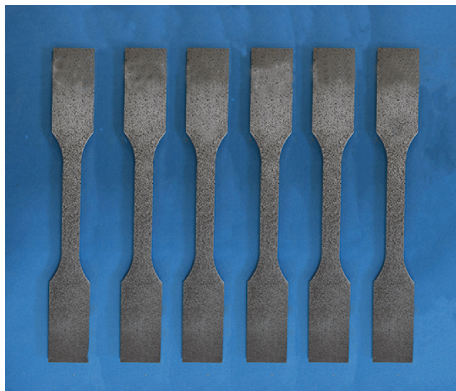


Cold-formed steel channel component

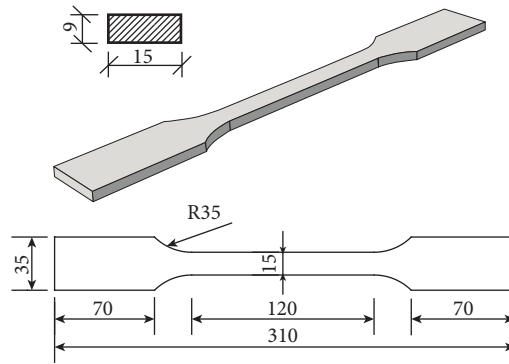
Flat and corner regions on steel channel

Diagram of flat and corner regions on steel channel

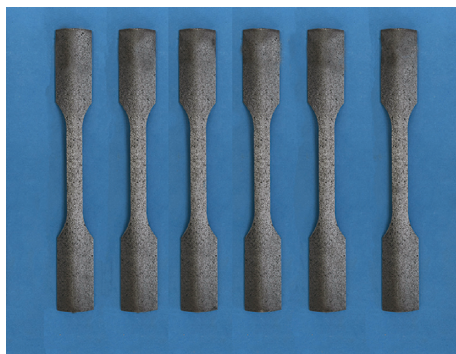
(a)



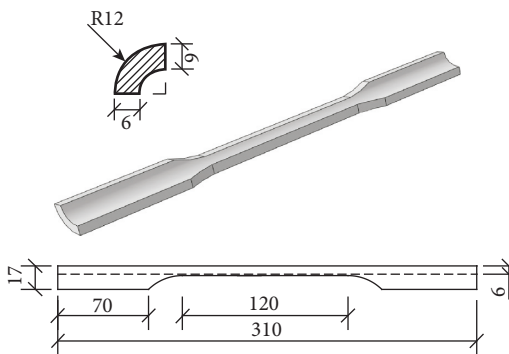
(b)



(c)



(d)



(e)

FIGURE 3: Fabrication and dimensions of flat and corner coupons from the cold-formed steel channel component: (a) flat and corner regions of cold-formed section; (b) flat coupons; (c) dimensions of flat coupon; (d) corner coupons; (e) dimensions of corner coupon.

tensile test, including the clear four phases of elastic phase, strain harden phase, diffuse necking phase, and localized necking phase, while for the corner specimens with the same wall thickness, the loads increase dramatically to peak capacity at the early displacement loading stage and then decrease obviously once exceeding the ultimate capacities. The load-displacement curves are basically divided into the four regions: the

elastic deformation, hardening, necking, and localized necking regions. It can be obtained that strain-hardening phenomenon was produced in the corner regions of the cold-formed section due to the cold-rolling working in the cold-formed section, which significantly improved the initial tensile stiffness of corner coupons but correspondingly reduced the plastic deformation and ductility performance.

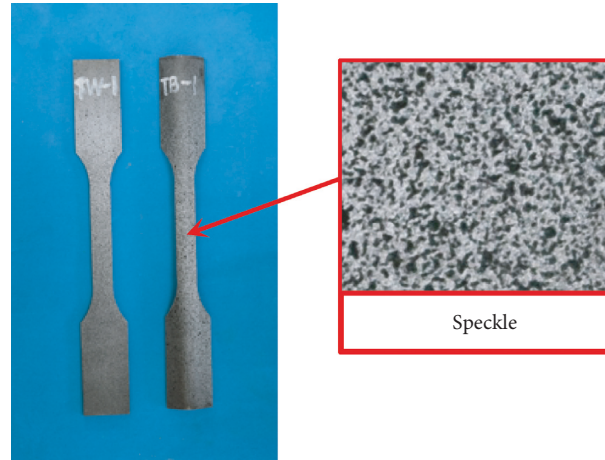


FIGURE 4: Speckle on coupon surfaces.

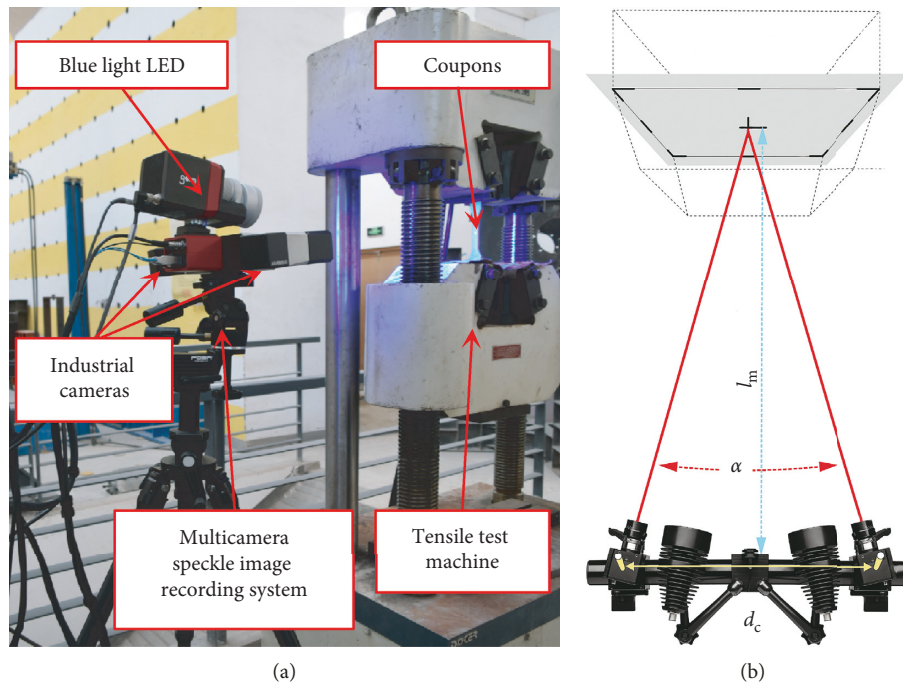


FIGURE 5: 3D speckle photography measurement system: (a) optical measurement setup; (b) diagram of optical measurement.

**3.2. Engineering Stress-Strain Curves of Flat and Corner Coupons.** Engineering stress-strain curve is conventionally used to describe the constitutive relationship, ignoring the reduction of cross-section area in calculation of section stress under uniaxial loading. For the flat coupons with a rectangular cross section, the initial thickness ( $d_{f0}$ ) was directly measured with 3D digital speckle scanning and the initial width of the center section ( $l_{f0}$ ) captured by an electronic vernier caliper as indicated in Figure 8(a) so that the initial cross-section area ( $A_{f0}$ ) was calculated and the engineering stress ( $\sigma_{fe}$ ) was obtained by equation (3). The gauge length ( $D_0$ ) of observed area was set as 120 mm for coupons, and the axial engineering strain values were directly captured. In this way, the engineering stress-strain curves of coupons (TW-1~TW-3 and BW-1~BW-3) were acquired as shown in

Figure 8(b). Similar to the flat coupons, as shown in Figure 8(c), the initial thickness ( $d_{c0}$ ) and the initial outer edge arc length ( $l_{c0}$ ) of corner coupons with a quarter circle cross section were measured using the 3D digital scanning method and the electronic vernier caliper, respectively. Thus, the initial section area ( $A_{c0}$ ) was obtained and the true stress ( $\sigma_{ce}$ ) was defined by equation (4). The engineering stress-strain curves of corner coupons (TB-1~TB-3 and BB-1~BB-3) were thereby determined as depicted in Figure 8(d).

$$\sigma_{fe} = \frac{F}{A_{f0}}, \quad (3)$$

$$\sigma_{ce} = \frac{F}{A_{c0}}. \quad (4)$$

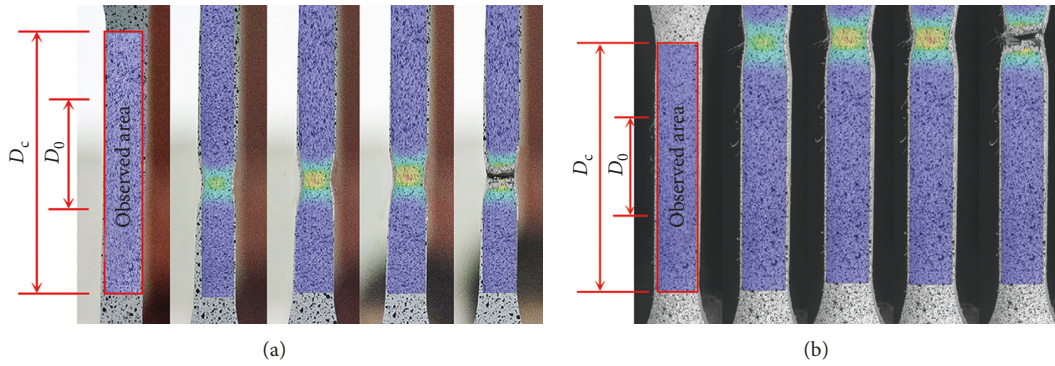


FIGURE 6: Strain nephograms of flat and corner coupons: (a) strain of flat coupon; (b) strain of corner coupon.

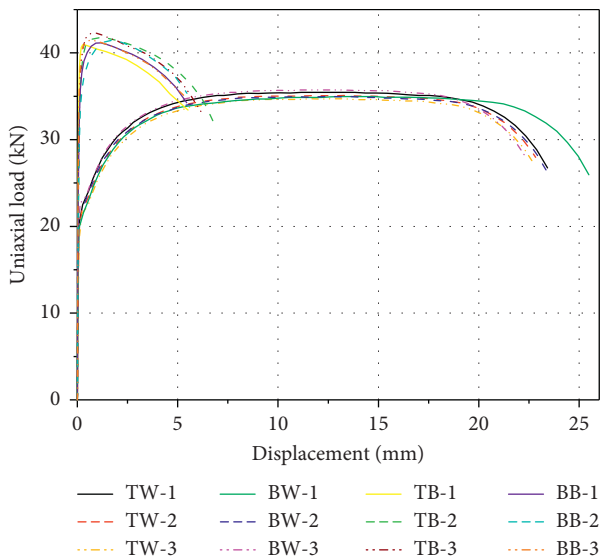


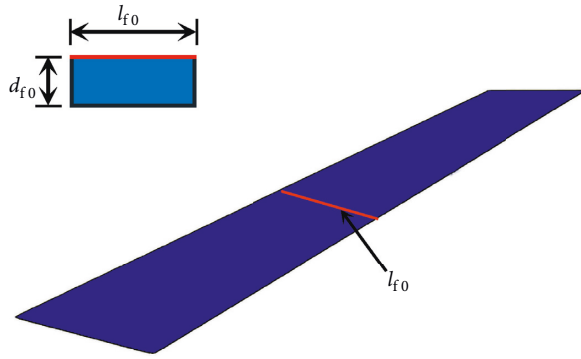
FIGURE 7: Load-displacement curves of flat and corner coupons.

It can be seen that the engineering stress-strain curves exhibit the similar features of the load-displacement curves. For the flat specimens, the curves are divided into four phases of the elastic phase, yielding phase, strengthening stage, and degradation stage. The clear yielding points and ultimate capacities are observed in this series of curves as shown in Figure 8(b). In contrast, there is no obvious yielding mark in the engineering curves of corner coupons as shown in Figure 8(d). For this type of stress-strain curve, the status with strain value of 0.2% is defined as the yielding strength [8]. The section stresses are developed rapidly to the ultimate strength point in the initial stage and then gradually decrease with the uniaxial strain increasing once the stresses exceed peak capacities. Figure 9 shows the comparison of the engineering stress-strain curves of flat specimens and corner specimens. Unsimilar to the flat specimens with steady strengthening, the corner specimens present significantly more dramatic stress reinforcement in the engineering stress-strain curves. With great tensile stiffness, the cross section stresses of corner coupons constantly grow to ultimate strength at the early strain developing stage compared with the flat coupons. Specifically, the engineering

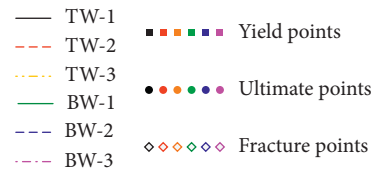
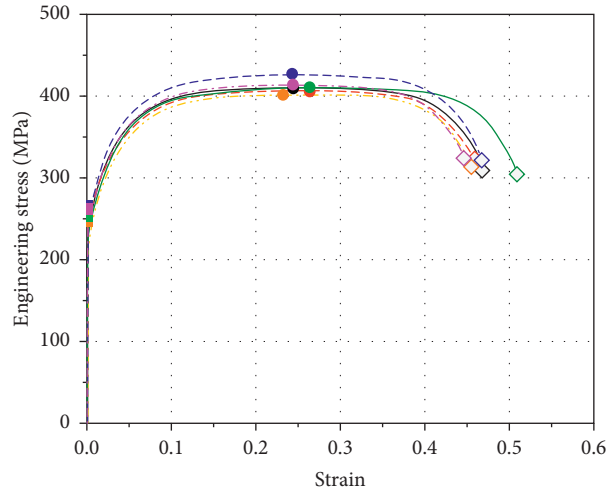
mechanical parameters of the flat and corner coupons are listed in Table 1. The yielding point was defined at the position where the slope of the stress-strain curve suddenly decreased so that the stress and strain values corresponding to the yielding point were defined as the yielding strength ( $\sigma_y$ ) and yielding strain ( $\epsilon_y$ ). Similarly, the ultimate strength ( $\sigma_u$ ) was determined as equal to stress value of the peak point and the corresponding strain value was denoted as ultimate strain ( $\epsilon_u$ ). Furthermore, the fracture strength ( $\sigma_f$ ) and fracture strain ( $\epsilon_f$ ) represent the stress and strain values of the fracture points, respectively. It is demonstrated in Table 1 that the average engineering yielding strength, yielding strain, ultimate strength, and fracture strength of corner coupons are 50.38%, 53.85%, 7.18%, and 13.67% higher while ultimate strain and fracture strain are 92.57% and 75.16% lower than those of flat specimens, respectively. It can be concluded that cold rolling leads to the strain hardening behavior of the corner regions in cold-formed sections, which highly improves the ultimate strength, but the plastic ductility is highly reduced, which results in the obviously lower ultimate strain and fracture strain than those of flat coupons.

### 3.3. True Stress-Strain Curves of Flat and Corner Coupons.

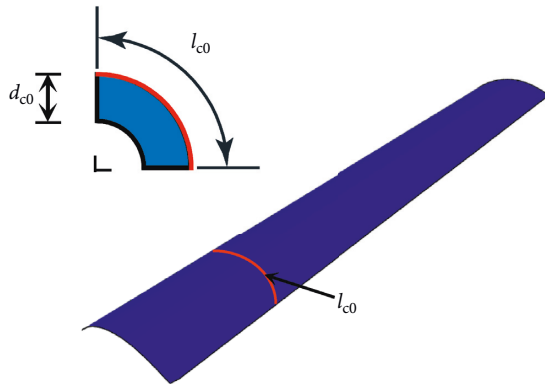
Compared with engineering stress-strain curves of flat and corner coupons, the true stress-strain curves, providing the true material mechanical performance in the whole strain range, are more significant for describing the material mechanical characteristics of the cold-formed section. The key point for the determination of the true stress-strain curve is to simultaneously capture the true cross-section area and the true axial strain during the full loading process. In this 3D digital image correlation measuring system, the width ( $l_f$ ) of the flat coupon with a rectangular cross section was directly measured during the whole loading process. This width value would exhibit a superior accuracy compared to the indirectly obtained real-time width by transverse strain timing the initial width because of the nonuniform distribution of cross section transverse strain as shown Figure 10(a). Meanwhile, the axial strain ( $\epsilon_{axial}$ ) and transverse strain ( $\epsilon_{trans}$ ) of observed area were individually calculated by  $\epsilon_{trans} = \Delta_l/l_c$  and  $\epsilon_{trans} = \Delta_w/w_c$ , where  $\Delta_l$ ,  $l_c$ ,  $\Delta_w$ , and  $w_c$  represent the real-time uniaxial extension,



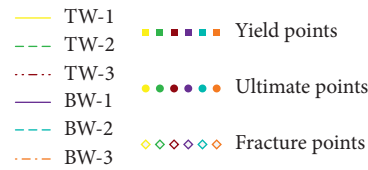
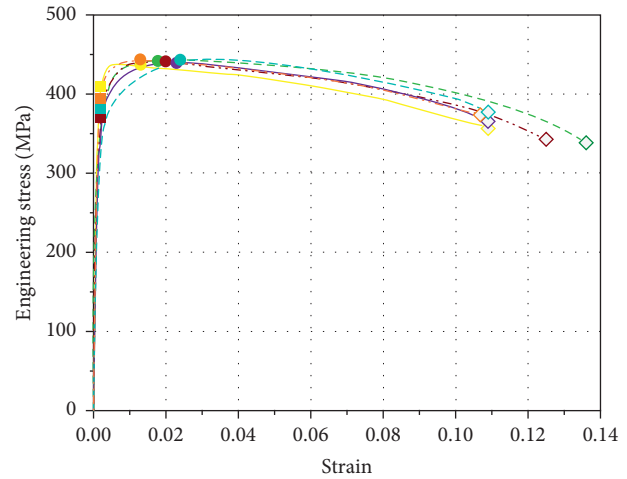
(a)



(b)



(c)



(d)

FIGURE 8: Measurement of engineering stress-strain curves: (a) diagram of initial section area measurement of flat coupon; (b) engineering stress-strain curves of flat coupons; (c) diagram of initial section area measurement of corner coupon; (d) engineering stress-strain curves of corner coupons.

uniaxial length, reduction of width, and width of calculated element area, respectively. On this basis, the multiaxial true strain field was described using the GOM software and the true axial and transverse strains can be directly captured. Assuming the steel coupons in this study were still isotropic and a uniaxial stress as well as strain state existed in the

necked region during the whole loading process, the true transverse strain was used to represent the strain in the thickness direction so that the true thickness was obtained by this way. Particularly, considering the nonuniformity of section strain distribution especially at the plastic stage, a total of ten gauging points were laid out on the necking cross

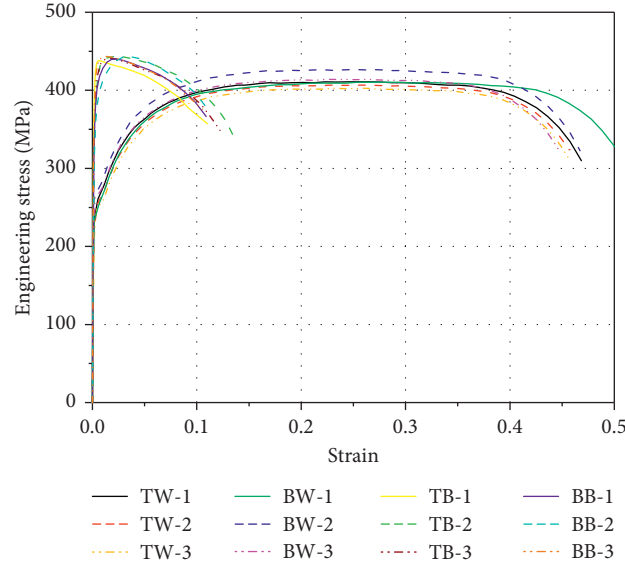


FIGURE 9: Comparison of engineering stress-strain curves of flat and corner coupons.

TABLE 1: Mechanical parameters of engineering stress-strain curves.

Types of coupons	Specimens	$\sigma_y$ (MPa)	$\varepsilon_y$	$\sigma_u$ (MPa)	$\varepsilon_u$	$\sigma_f$ (MPa)	$\varepsilon_f$
Flat coupons	TW-1	260.64	0.0013	410.77	0.244	309.76	0.468
	TW-2	254.26	0.0012	406.66	0.264	323.79	0.457
	TW-3	247.88	0.0012	402.55	0.232	313.507	0.455
	BW-1	253.58	0.0013	410.42	0.264	304.76	0.509
	BW-2	265.67	0.0013	426.44	0.243	322.272	0.467
	BW-3	261.97	0.0012	413.91	0.244	323.81	0.447
Corner coupons	TB-1	410.62	0.002	437.99	0.013	357.15	0.109
	TB-2	383.75	0.002	441.94	0.018	338.52	0.136
	TB-3	370.78	0.002	441.35	0.02	343.64	0.125
	BB-1	380.78	0.002	440.13	0.023	366.35	0.109
	BB-2	380.78	0.002	443.23	0.024	377.68	0.109
	BB-3	395.22	0.002	443.44	0.013	373.94	0.107
Average values of flat coupons		257.33	0.0013	411.79	0.249	316.32	0.467
Average values of corner coupons		386.99	0.002	441.35	0.0185	359.55	0.116
Improvements of average values		50.38%	53.85%	7.18%	-92.57%	13.67%	-75.16%

Note. (1)  $\sigma_y$  is the yielding strength; (2)  $\varepsilon_y$  is the yielding strain; (3)  $\sigma_u$  is the ultimate strength; (4)  $\varepsilon_u$  is the corresponding ultimate strain; (5)  $\sigma_f$  is the fracture stress; and (6)  $\varepsilon_f$  is the fracture strain.

section to capture the average longitudinal and transverse strain as indicated in Figure 10(b). Thus, the average thicknesses ( $d_f$ ) was obtained and the true cross-section area ( $A_f$ ) in the full displacement loading range was defined as presented in Figure 10(c) so that the true stress can be calculated by equation (5). Therefore, the true stress-strain curves of flat coupons were determined, including the elastic stage and two strain hardening stages, as demonstrated in Figure 10(d). Similarly, the real-time outer edge arch ( $l_c$ ) of corner coupons was directly gauged as shown in Figure 11(a). In addition, the average longitudinal and transverse strains of the ten gauging points were obtained as indicated in Figure 11(b) so that the true area ( $A_c$ ) was defined and the true stress was captured by equation (6). Thus, the true stress-strain curves of corner coupons without obvious yielding point were obtained, containing the elastic

phase, strengthening phase, and horizontal phase, as shown in Figure 11(d).

$$\sigma_{ft} = \frac{F}{A_f}, \quad (5)$$

$$\sigma_{ct} = \frac{F}{A_c}. \quad (6)$$

Figure 12 shows the comparison between engineering stress-strain curves and true stress-strain curves of flat and corner coupons. As revealed in Figure 12(a), the two types of stress-strain curves of flat specimens are basically consistent at the initial stage. Once the uniaxial stress value run up to the nominal ultimate capacity, the gradual strength degradation happen in engineering curves while the continuously enhanced strength occurs in true curves so that the

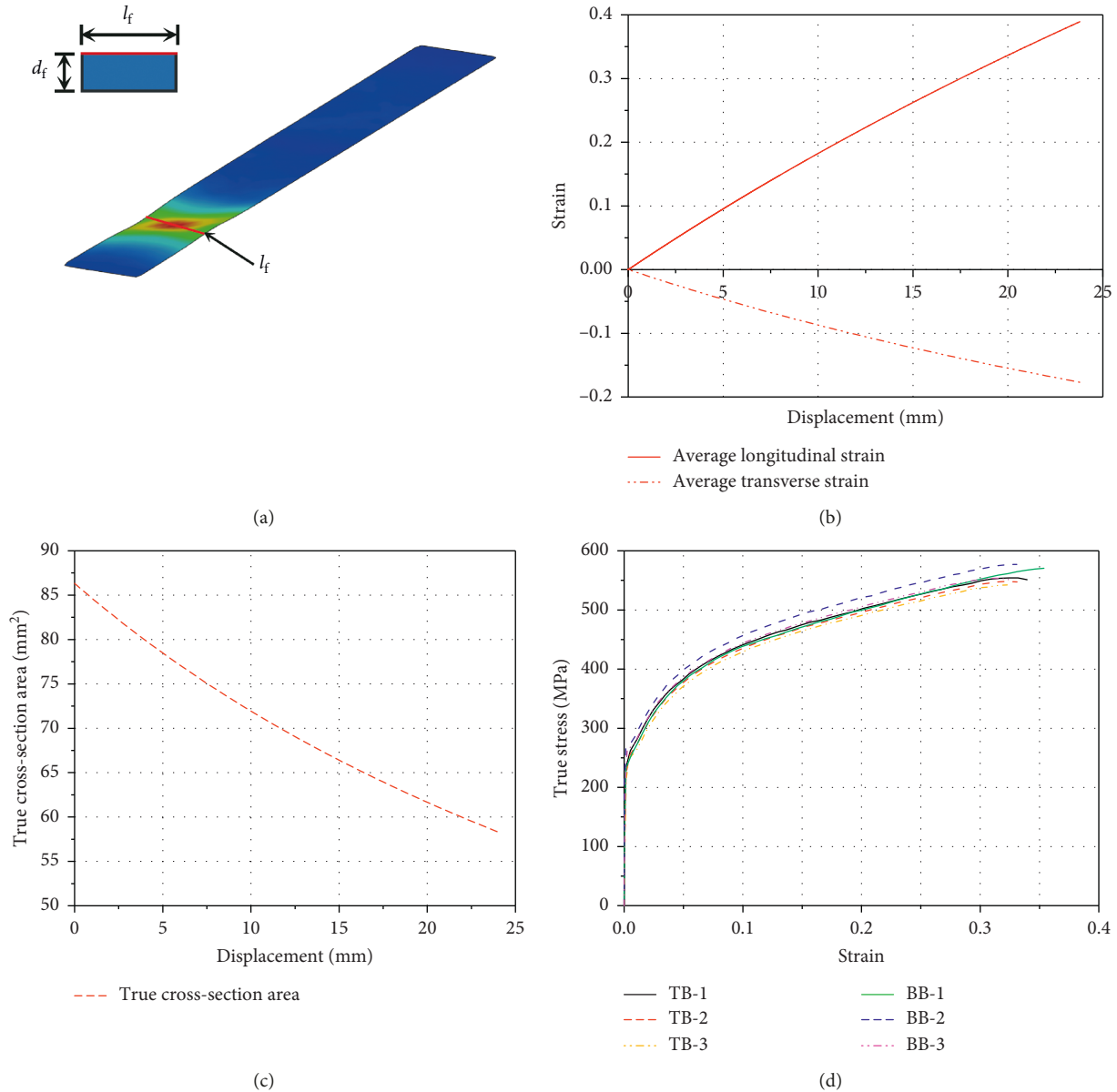


FIGURE 10: Capture of true stress-strain curves of flat coupon: (a) diagram of real-time section area capture of flat coupon; (b) average strain; (c) true cross-section area; (d) true stress-strain curves of flat coupons.

increasingly obvious gaps between true stresses and engineering stresses are observed with the strain increasing. The material mechanical parameters of engineering and true stress-strain curves of the flat coupon are listed in Table 2. It is shown that there is little difference in the average yielding stress between engineering and true curves. However, the average true yielding strain of flat specimens is 7.69% lower than the engineering value. The numerous digital speckle images were consistently captured in the DIC system, and then the engineering strain values were directly obtained using the GOM software based on the nominal strain calculation principle ( $\epsilon_n = D/D_0$ ). Moreover, the true strain values up to the point of maximum force were captured by  $\epsilon_t = D/D_L$ , and a local point measurement in the necked region was used to express true strain in the DIC

measurement system once necking has initiated. It is noted that the engineering strains ( $\epsilon_n$ ) were obtained by the real-time displacement ( $D$ ) and initial gauge length ( $D_0$ ) while the true strains ( $\epsilon_t$ ) were obtained by the real-time displacement ( $D$ ), real-time gauge length ( $D_L$ ), and local point strain value in the necked region so that the average true yielding strain is lower than the engineering value. Furthermore, the true ultimate strength is 35.40% higher and the ultimate strain, defined by the strain value corresponding to ultimate strength, is 32.13% higher than engineering values, respectively. Comparatively, as shown in Figure 12(b), the true and engineering stress-strain curves of corner coupons basically are kept consistent, and the true strength exhibits a slight improvement compared with the engineering value in the descent stage. As summarized in

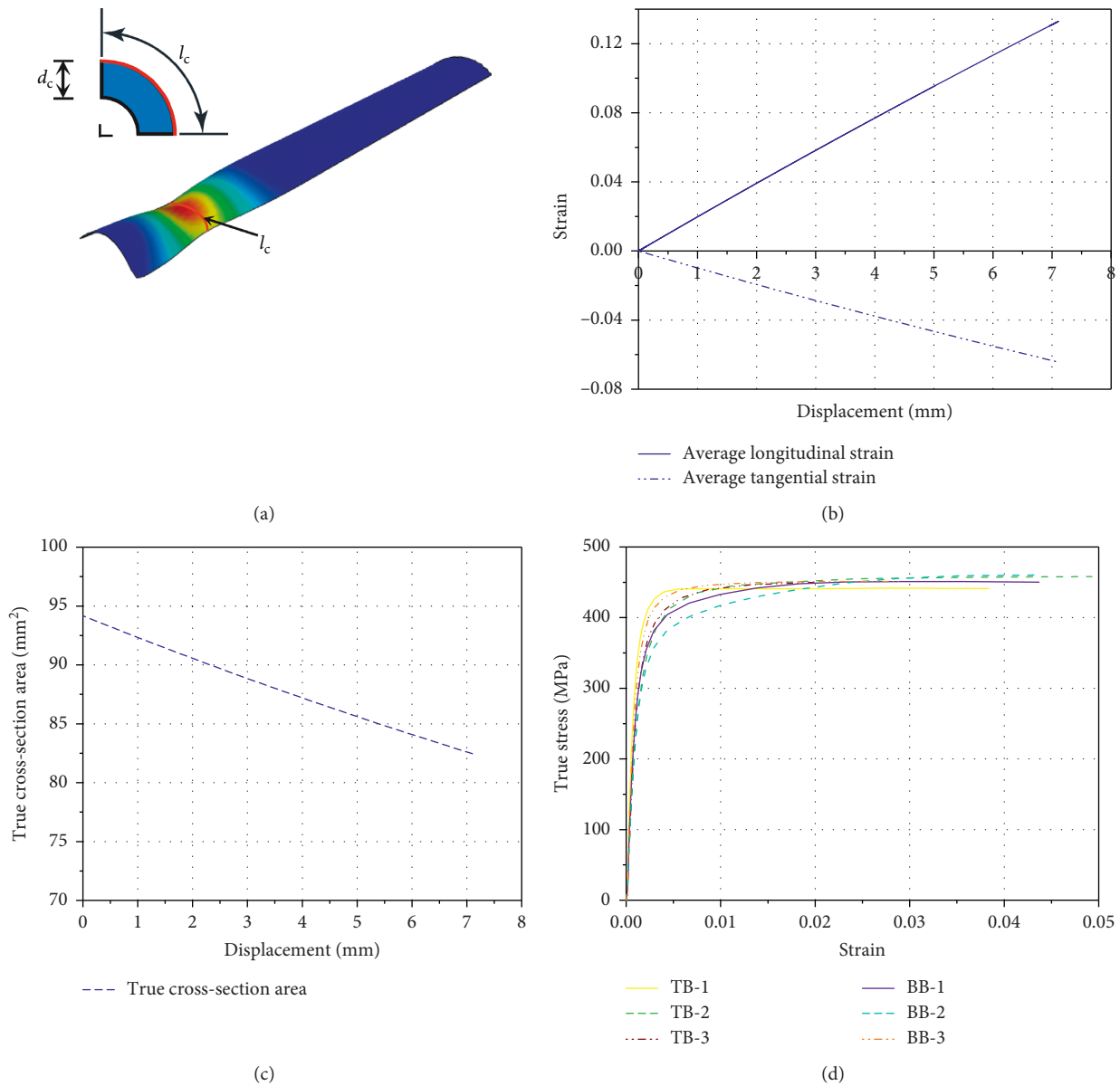


FIGURE 11: Capture of true stress-strain curves of corner coupon: (a) diagram of real-time section area capture of corner coupon; (b) average strain; (c) true cross-section area; (d) true stress-strain curves of corner coupons.

Table 3, the true yielding stress defined as stress value of 0.2% strain is in great agreement with the engineering yielding stress. Moreover, the true ultimate strength, ultimate strain, and fracture stress are 2.44%, 62.16%, and 11.59% greater, respectively. The true fracture strain is 3.45% lower than that of engineering constitute curves directly obtained using GOM software based on the nominal strain calculation principle and true strain calculation principle, individually. In addition, the relationships between true and engineering strains for flat and corner specimens are presented in Figures 12(c) and 12(d). It can be concluded that without considering the reduction of cross-section area, the gradual strength deterioration is observed in the declining phases of engineering stress-strain curves of flat specimens, while for the true stress-strain curves of flat regions, the stress was

calculated based on the real-time section area and the true longitudinal strain was directly measured. Considering the section area reduction in the whole loading process, the tensile strain hardening is indicated in this series of curves, which leads to the constant enhancement of strength with the uniaxial strain increasing so that the true ultimate strengths of the true stress-strain curves of flat coupons exhibit the significant improvements compared with the engineering ultimate strengths. For the corner regions in cold-formed sections, the plastic deformation and ductility are highly restrained due to the cold-working effect. Thus, the strength-heightening phenomenon of corner regions at a high strain level is clearly limited, which results in the slight increase of ultimate strength of true stress-strain curves than that of engineering curves.

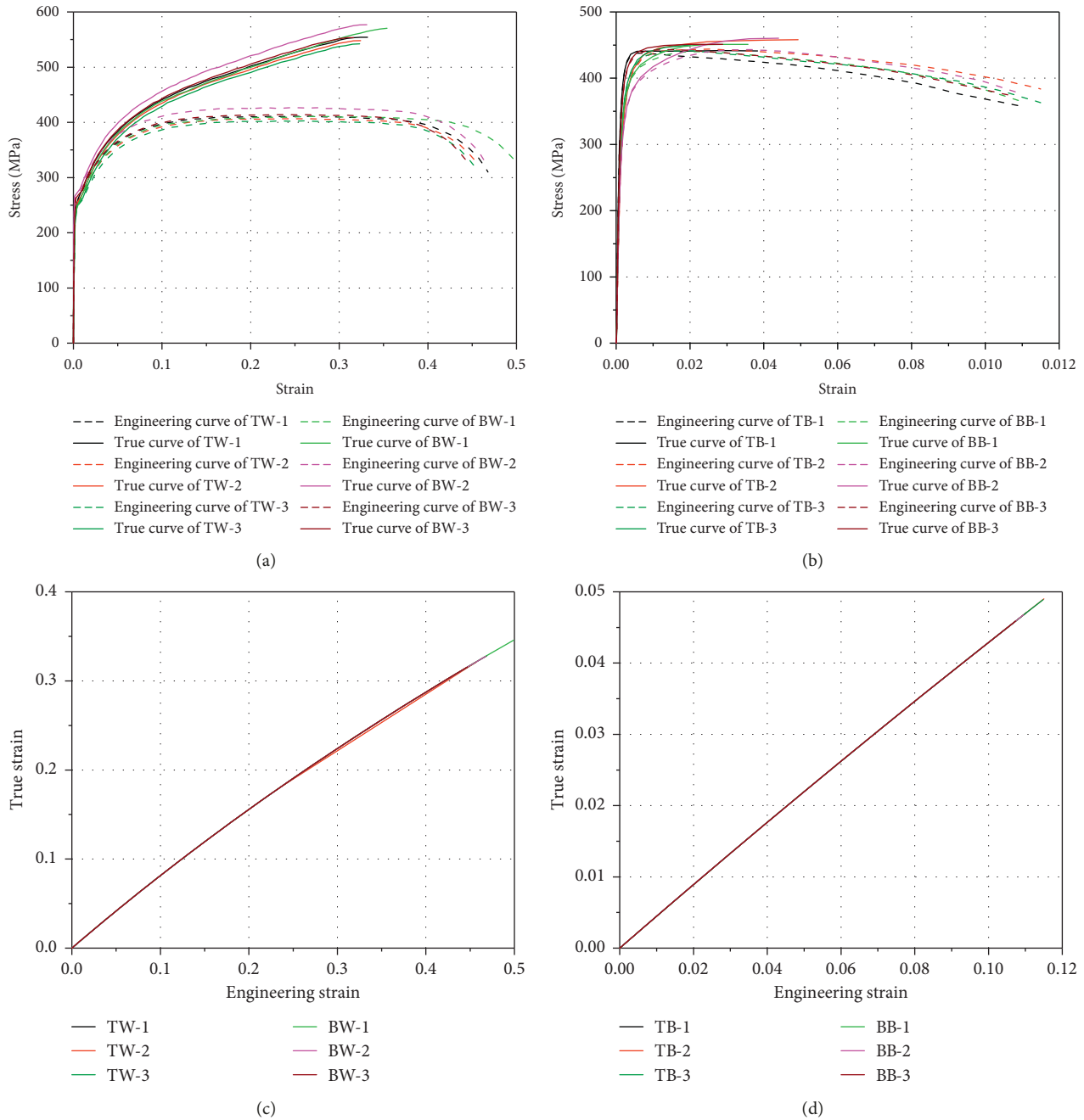


FIGURE 12: Comparison of true and engineering stress-strain curves of flat and corner coupons: (a) true and engineering stress-strain curves of flat coupons; (b) true and engineering stress-strain curves of corner coupons; (c) relationship between true and engineering strains of flat coupons; (d) relationship between true and engineering strains of corner coupons.

The comparison of the true stress-strain curves of flat and corner regions is illustrated in Figure 13 to evaluate the effect of cold-working action on the true material mechanical performance of the cold-formed section. The true yielding strengths of corner specimens are obviously higher compared with flat specimens. In addition, the strength-enhancing phenomenon is observed in true curves of flat specimens with the strain increasing, while the stresses of corner specimens gradually decrease to fracture strength at a relatively lower strain level due to the serious reduction of

ductility. Specifically, as listed in Table 4, the average true yielding strength and yielding strain of corner specimens are 52.83% and 61.54% higher than those of flat specimens, while the average true ultimate strength and ultimate strain are 18.91% and 90.88% lower compared with the flat specimens, respectively. It can be captured that considering the reduction of cross-section area under uniaxial loading, the continuous tensile strain-hardening phenomenon is observed on flat regions in the cold-formed section at the plastic deformation stage. This leads to the true stress of flat

TABLE 2: Mechanical parameters of engineering and true stress-strain curves of flat coupons.

Types of curves	Specimens	$\sigma_y$ (MPa)	$\epsilon_y$	$\sigma_u$ (MPa)	$\epsilon_u$	$\sigma_f$ (MPa)	$\epsilon_f$
Engineering stress-strain curves	TW-1	260.64	0.0013	410.77	0.244	309.76	0.468
	TW-2	254.26	0.0012	406.66	0.264	323.79	0.457
	TW-3	247.88	0.0012	402.55	0.232	313.507	0.455
	BW-1	253.58	0.0013	410.42	0.264	304.76	0.509
	BW-2	265.67	0.0013	426.44	0.243	322.272	0.467
	BW-3	261.97	0.0012	413.91	0.244	323.81	0.447
True stress-strain curves	TW-1	262.033	0.0012	554.07	0.332	—	—
	TW-2	255.463	0.0011	548.14	0.324	—	—
	TW-3	262.68	0.0011	542.26	0.323	—	—
	BW-1	255.13	0.0012	570.56	0.354	—	—
	BW-2	266.04	0.0012	576.83	0.331	—	—
	BW-3	262.63	0.0011	553.42	0.308	—	—
Average values of engineering curves		257.33	0.0013	411.79	0.249	316.32	0.467
Average values of true curves		260.66	0.0012	557.55	0.329	—	—
Improvements of average values		1.29%	-7.69%	35.40%	32.13%	—	—

TABLE 3: Mechanical parameters of engineering and true stress-strain curves of corner coupons.

Types of curves	Specimens	$\sigma_y$ (MPa)	$\epsilon_y$	$\sigma_u$ (MPa)	$\epsilon_u$	$\sigma_f$ (MPa)	$\epsilon_f$
Engineering stress-strain curves	TB-1	410.62	0.002	437.99	0.013	357.15	0.109
	TB-2	383.75	0.002	441.94	0.018	338.52	0.136
	TB-3	370.78	0.002	441.35	0.02	343.64	0.125
	BB-1	380.78	0.002	440.13	0.023	366.35	0.109
	BB-2	380.78	0.002	443.23	0.024	377.68	0.109
	BB-3	395.22	0.002	443.44	0.013	373.94	0.107
True stress-strain curves	TB-1	411.55	0.002	441.59	0.028	396.57	0.105
	TB-2	384.96	0.002	458.03	0.039	384.67	0.128
	TB-3	392.64	0.002	450.32	0.021	386.67	0.128
	BB-1	404.35	0.002	451.08	0.029	406.28	0.103
	BB-2	382.45	0.002	460.51	0.034	419.02	0.104
	BB-3	414.21	0.002	451.09	0.029	414.09	0.102
Average values of engineering curves		386.99	0.002	441.35	0.0185	359.55	0.116
Average values of true curves		398.36	0.002	452.10	0.03	401.22	0.112
Improvements of average values		2.94%	0%	2.44%	62.16%	11.59%	-3.45%

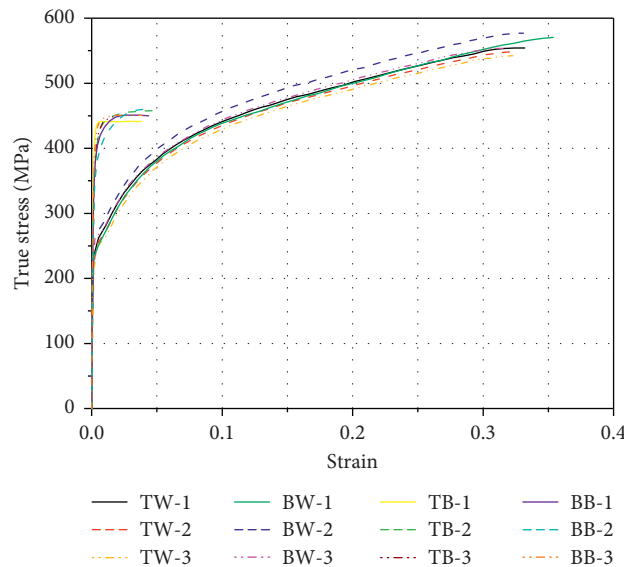


FIGURE 13: Comparison of true stress-strain curves of flat and corner coupons.

TABLE 4: Mechanical parameters of true stress-strain curves.

Types of coupons	Specimens	$\sigma_{ty}$ (MPa)	$\epsilon_{ty}$	$\sigma_{tu}$ (MPa)	$\epsilon_{tu}$	$\sigma_{tf}$ (MPa)	$\epsilon_{tf}$
Flat coupons	TW-1	262.033	0.0013	554.07	0.332	—	—
	TW-2	255.463	0.0012	548.14	0.324	—	—
	TW-3	262.68	0.0012	542.26	0.323	—	—
	BW-1	255.13	0.0013	570.56	0.354	—	—
	BW-2	266.04	0.0013	576.83	0.331	—	—
	BW-3	262.63	0.0012	553.42	0.308	—	—
	TB-1	411.55	0.002	441.59	0.028	396.57	0.105
Corner coupons	TB-2	384.96	0.002	458.03	0.039	384.67	0.128
	TB-3	392.64	0.002	450.32	0.021	386.67	0.128
	BB-1	404.35	0.002	451.08	0.029	406.28	0.103
	BB-2	382.45	0.002	460.51	0.034	419.02	0.104
	BB-3	414.21	0.002	451.09	0.029	414.09	0.102
	Average values of flat coupons	260.66	0.0013	557.55	0.329	—	—
Average values of corner coupons	398.36	0.002	452.10	0.030	401.22	0.112	
Improvements of average values	52.83%	61.54%	-18.91%	-90.88%	—	—	

Note. (1)  $\sigma_{ty}$  is the true yielding strength; (2)  $\epsilon_{ty}$  is the true yielding strain; (3)  $\sigma_{tu}$  is the true ultimate strength; (4)  $\epsilon_{tu}$  is the corresponding true ultimate strain; (5)  $\sigma_{tf}$  is the true fracture stress; and (6)  $\epsilon_{tf}$  is the true fracture strain.

regions continuously strengthened as the strain exceeds the yielding strain. Compared with flat regions, the cold-working strain hardening-phenomenon occurs on the corner regions so that the true stress of corner coupons dramatically increases to the ultimate strength at a relatively low strain value. However, the ductility performance of corner regions is intensively reduced due to cold-rolling behavior, which greatly limits the strength enhancement of corner specimens at the plastic strain phase. Thus, the flat regions exhibit the greater true ultimate strength.

## 4. Simplified Multilinear Models of True Stress-Strain Curves

**4.1. Trilinear Model with Two-Stage Strain Hardening for Flat Region.** According to the features of the accurate true stress-strain curves measured using the 3D DIC method, simplified multilinear constitutive models were established to describe the true material performance of flat and corner regions in the cold-formed section so that the numerical analysis of cold-formed steel structural models can be performed accurately and effectively.

It was seen from the true stress-strain curves of flat regions shown in Figure 14(a) that the obvious yielding points can be observed but the yielding platforms were not exhibited evidently. Considering the reduction of cross-section areas, the two-stage tensile strain hardening behavior occurred at the plastic strain stage, and the dramatic strength deterioration phenomenon was observed once the stress run up to the ultimate capacity. Therefore, the simplified trilinear model with two-stage strain hardening was proposed as shown in Figure 14(a) based on the typical characters of true stress-strain curves of flat coupons. Yun and Gardner [17] proposed the standardized quad-linear material model, representing the yielding plateau and two-stage strain-strengthening phenomenon, to describe the simplified

stress-strain relationship of hot-rolled steels, and the simplified constitutive expression was obtained as

$$f(\epsilon) = \begin{cases} E\epsilon, & \epsilon \leq \epsilon_y, \\ f_y, & \epsilon_y < \epsilon \leq \epsilon_{sh}, \\ f_y + E_{sh}(\epsilon - \epsilon_{sh}), & \epsilon_{sh} < \epsilon \leq C_1\epsilon_u, \\ f_{C_1\epsilon_u} + \frac{f_u - f_{C_1\epsilon_u}}{\epsilon_u - C_1\epsilon_u}(\epsilon - C_1\epsilon_u), & C_1\epsilon_u < \epsilon \leq \epsilon_u, \end{cases} \quad (7)$$

where  $E$ ,  $f_y$ ,  $f_u$ ,  $\epsilon_u$ ,  $C_1\epsilon_u$ , and  $f_{C_1\epsilon_u}$  represent the elastic module, the yielding strength, the ultimate strength, the corresponding strain at ultimate capacity status, the strain at intersection point of the third stage of the model, and the corresponding stress value, respectively. Figure 14(b) shows the standardized secondary hardening trilinear constitutive model for flat regions in the cold-formed section, presenting the two-stage hardening behavior as well as eliminating the yielding plateau. Correspondingly, the analytical expression as equation (8) for the simplified three-stage true stress-strain model was obtained together with the experimental results:

$$f(\epsilon) = \begin{cases} E\epsilon, & \epsilon \leq \epsilon_y, \\ f_y + \frac{f_{0.23\epsilon_u} - f_y}{0.23\epsilon_u - \epsilon_y}(\epsilon - \epsilon_y), & \epsilon_y < \epsilon \leq 0.23\epsilon_u, \\ f_{0.23\epsilon_u} + \frac{f_u - f_{0.23\epsilon_u}}{\epsilon_u - 0.23\epsilon_u}(\epsilon - 0.23\epsilon_u), & 0.23\epsilon_u < \epsilon \leq \epsilon_u. \end{cases} \quad (8)$$

**4.2. Simplified Trilinear Model for Corner Region.** As for the practical mechanical property of corner regions in the

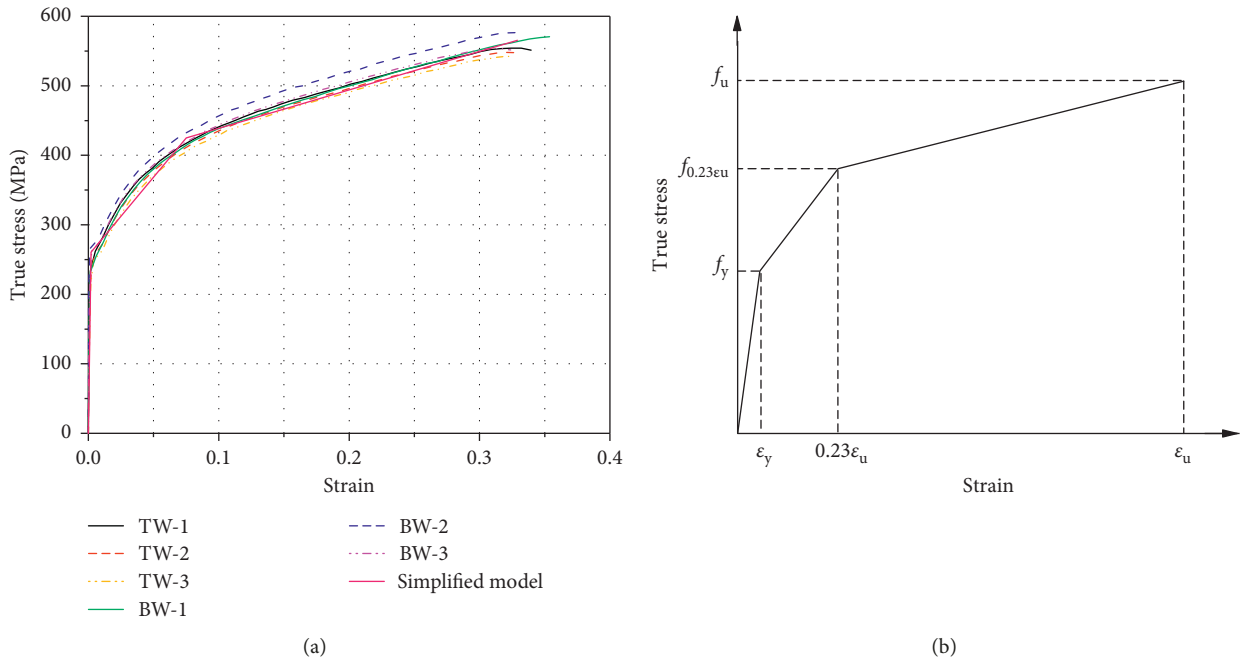


FIGURE 14: Simplified model of true stress-strain curve of the flat region: (a) features of true stress-strain curves of the flat region; (b) trilinear constitutive model with two-stage strain hardening for the flat region.

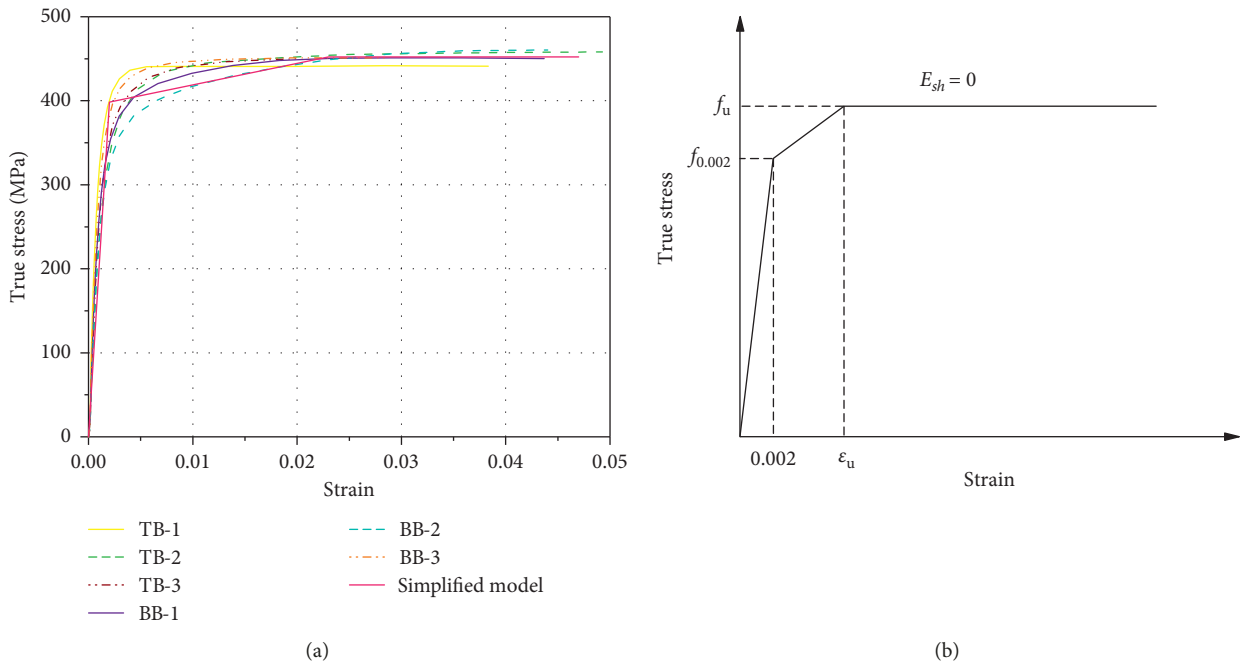


FIGURE 15: Simplified model of true stress-strain curve of the corner region: (a) features of true stress-strain curves of the corner region; (b) trilinear constitutive model for the corner region.

cold-formed section, it is shown in Figure 15(a) that there was no clear yielding marks in true stress-strain curves, and yielding strength was highly improved due to the cold-rolling working. The Ramberg–Osgood model [29] is generally used to describe this type of stress-strain curves of metallic materials, and the basic material parameters including the elastic modulus  $E$ , the

0.2% stress  $\sigma_{0.2}$  as the equivalent yielding strength and the strain hardening exponent  $n$  are defined in this analytical model. For the direct application of the true stress-strain relationship of the corner region in design calculations of cold-formed components, a trilinear model was established in this paper based on the features of measured true stress-strain



FIGURE 16: FE models of flat and corner coupons: (a) flat coupon; (b) corner coupon.

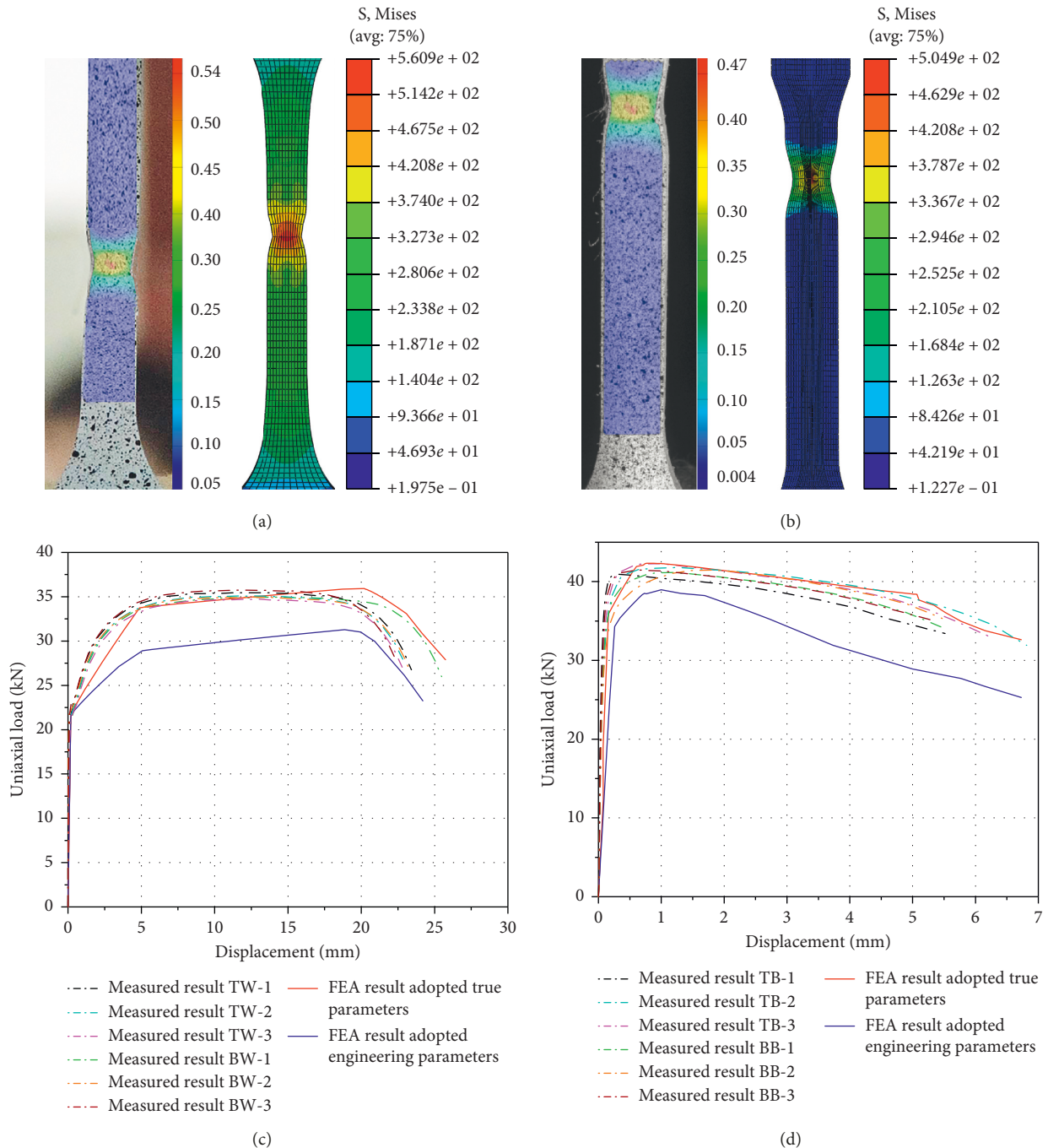


FIGURE 17: Comparison of numerical and experimental results: (a) failure states of flat coupon; (b) failure states of corner coupon; (c) load-displacement curves of flat coupon; (d) load-displacement curves of corner coupon.

curves as shown in Figure 15(a). Figure 15(b) shows the standardized trilinear model for the corner regions in cold-formed sections, and the three-stage expression is defined as

$$f(\varepsilon) = \begin{cases} E\varepsilon, & \varepsilon \leq \varepsilon_y, \\ f_{0.002} + \frac{f_u - f_{0.002}}{\varepsilon_u - 0.002} (\varepsilon - 0.002), & \varepsilon_y < \varepsilon \leq \varepsilon_u, \\ f_u, & \varepsilon_u < \varepsilon \leq \varepsilon_f. \end{cases} \quad (9)$$

## 5. Verification of True Stress-Strain Curves of Flat and Corner Regions

**5.1. Numerical Modelling.** Finite element analysis (FEA) was performed to verify the reliability of the 3D digital image correlation measuring method and the simplified models of the true stress-strain curves of flat and corner regions in the cold-formed section. As shown in Figure 16, the prototypical 3D numerical models of flat and corner coupons consistent with experimental specimens were built using C3D8R solid elements. In addition, the end constraints and uniaxial displacement loading on FE models were set in complete agreement with that in tests. Particularly, the trilinear constitutive model with two-stage strain hardening and simplified trilinear constitutive model, together with measured results of the digital image correlation system, were assigned to flat and corner models, respectively. In this way, the simulated results were obtained for comparison.

**5.2. Comparison of Load-Displacement Curves.** Figures 17(a) and 17(b) show a comparison of the experimental and predicted strain distribution and deformation of flat and corner coupons under the same loading conditions, which present the superior agreement in the failure modes of experimental and numerical results. As shown in Figures 17(c) and 17(d), the FEA results of flat and corner coupons with true constitutive models were compared with all test data, respectively, which exhibit a great agreement. Furthermore, the numerical load-displacement curves which adopted the true stress-strain model fit very well with the measured curves but the obvious difference between FEA results adopted the engineering stress-strain model and test results can be observed. This highly proves the reliability of the simplified true constitutive models of flat and corner regions in the cold-formed section and validates the dependability of the optic measurement of true stress-strain curves using the 3D digital image correlation method.

## 6. Conclusions

To evaluate the true stress-strain curves of flat and corner regions of the cold-formed channel section, a series of coupon tests with the multicamera DIC system were carried out in this study. The features of true stress-strain curves were compared with those of engineering stress-strain curves, and the practical material mechanical performance of flat and corner

regions was discussed comparatively. Together with the optical measuring results, a trilinear model with two-stage strain hardening and a simplified trilinear model were proposed for representing the true stress-strain curves of flat and corner regions. Moreover, the FEA was performed for verifying the DIC method and the simplified true constitutive models. The following are the major conclusions:

- (1) In the cold-formed channel section with wall thickness of 6 mm, the load-displacement curves of flat and corner coupons can be divided into four typical phases of the elastic phase, hardening phase, necking phase, and localized necking phase.
- (2) Considering the section area reduction during the loading process, the obvious difference between the true and engineering stress-strain curves of the flat region was captured. The secondary tensile strain-hardening phenomenon in the true stress-strain curves of flat coupons was observed at the large strain stage, which leads to the significant enhancement of true ultimate strength compared with the engineering ultimate strength. The assumptions of isotropic behavior together with uniaxial stress and strain state were accounted in this study, and the effect of those assumptions will be studied in future.
- (3) For the corner regions in cold-formed sections, the plastic deformation was obviously restrained due to the cold-working behavior. The tensile strain hardening at plastic status is thereby limited so that there is no obvious difference between the true and engineering stress-strain curves of corner coupons.
- (4) The true yielding strength of the corner region is intensively promoted compared with the flat region, but the ultimate strength is relatively lower due to the plastic hardening action restrained.
- (5) The trilinear model with two-stage strain hardening and the simplified trilinear model were proposed to represent the true stress-strain curves of flat and corner regions individually.
- (6) The comparison of numerical and experimental results effectively verified the reliability of the 3D digital image correlation method and the dependability of the multilinear constitutive models for the flat and corner regions in this paper.

## Data Availability

The data used to support the findings of this study are included within the article.

## Conflicts of Interest

The authors declare no conflicts of interest.

## Acknowledgments

This research was funded by the Fundamental Research Funds for the Central Universities (Grant no. 2018ZDPY04)

and the Doctoral Research Fund of Jiangsu Collaborative Innovation Center for Building Energy Saving and Construction Technology (Grant nos. SJXTBS1720 and SJXTBS1721).

## References

- [1] S. Afshan, B. Rossi, and L. Gardner, "Strength enhancements in cold-formed structural sections—part I: material testing," *Journal of Constructional Steel Research*, vol. 83, pp. 177–188, 2013.
- [2] B. Rossi, S. Afshan, and L. Gardner, "Strength enhancements in cold-formed structural sections—Part II: predictive models," *Journal of Constructional Steel Research*, vol. 83, pp. 189–196, 2013.
- [3] B. Xu, F. Wu, and G. Xu, "Mechanism study on the axial compressive performance of short square CFST columns with different stiffeners," *Advances in Civil Engineering*, vol. 2018, Article ID 9109371, 10 pages, 2018.
- [4] G.-W. Li and Y.-Q. Li, "Overall stability behavior of axially compressed cold-formed thick-walled steel tubes," *Thin-Walled Structures*, vol. 125, pp. 234–244, 2018.
- [5] B. Young and K. J. R. Rasmussen, "Behaviour of cold-formed singly symmetric columns," *Thin-Walled Structures*, vol. 33, no. 2, pp. 83–102, 1999.
- [6] J. Xia, H. Chang, H. Goldsworthy, Y. Bu, and Y. Lu, "Axial hysteretic behavior of doubler-plate reinforced square hollow section tubular T-joints," *Marine Structures*, vol. 55, pp. 162–181, 2017.
- [7] S. Torabian, D. C. Fratamico, and B. W. Schafer, "Experimental response of cold-formed steel Zee-section beam-columns," *Thin-Walled Structures*, vol. 98, pp. 496–517, 2016.
- [8] J. Wang, G. Shu, B. Zheng, and Q. Jiang, "Investigations on cold-forming effect of cold-drawn duplex stainless steel tubular sections," *Journal of Constructional Steel Research*, vol. 152, pp. 81–93, 2019.
- [9] L. Gardner, N. Saari, and F. Wang, "Comparative experimental study of hot-rolled and cold-formed rectangular hollow sections," *Thin-Walled Structures*, vol. 48, no. 7, pp. 495–507, 2010.
- [10] H. Chang, J. Xia, Z. Guo, C. Hou, W. Din, and F. Qin, "Experimental study on the axial compressive strength of vertical inner plate reinforced square hollow section T-joints," *Engineering Structures*, vol. 172, pp. 131–140, 2018.
- [11] M. K. Howlader, J. Marik, and M. Jandera, "Cold-forming effect on stainless steel sections," *International Journal of Steel Structures*, vol. 16, no. 2, pp. 317–332, 2016.
- [12] W. F. Maia, L. C. M. Vieira, B. W. Schafer, and M. Malite, "Experimental and numerical investigation of cold-formed steel double angle members under compression," *Journal of Constructional Steel Research*, vol. 121, pp. 398–412, 2016.
- [13] Y. H. Lee, Y. L. Lee, and C. S. Tan, "Experimental investigation on cold-formed steel beams under pure bending," *Jurnal Teknologi*, vol. 58, no. 1, pp. 13–20, 2012.
- [14] K. Wang, J. Xia, X. Chen, B. Xu, X. Liang, and J. Wang, "Performance of the cold-bending channel-angle buckling-restrained brace under cyclic loading," *Advances in Civil Engineering*, vol. 2019, Article ID 9710529, 12 pages, 2019.
- [15] X. Chen, J. Xia, B. Xu, and R. Ma, "Performance of a novel built-up column composed of four cold-formed tubes," *Proceedings of the Institution of Civil Engineers—Structures and Buildings*, vol. 9, pp. 1–16, 2019.
- [16] M. Kamaya and M. Kawakubo, "True stress-strain curves of cold worked stainless steel over a large range of strains," *Journal of Nuclear Materials*, vol. 451, no. 1–3, pp. 264–275, 2014.
- [17] X. Yun and L. Gardner, "Stress-strain curves for hot-rolled steels," *Journal of Constructional Steel Research*, vol. 133, pp. 36–46, 2017.
- [18] E. E. Cabezas and D. J. Celentano, "Experimental and numerical analysis of the tensile test using sheet specimens," *Finite Elements in Analysis and Design*, vol. 40, no. 5–6, pp. 555–575, 2004.
- [19] Z. L. Zhang, M. Hauge, J. Ødegård, and C. Thaulow, "Determining material true stress-strain curve from tensile specimens with rectangular cross-section," *International Journal of Solids and Structures*, vol. 36, no. 23, pp. 3497–3516, 1999.
- [20] H. C. Hyun, M. Kim, S. Bang, and H. Lee, "On acquiring true stress-strain curves for sheet specimens using tensile test and FE analysis based on a local necking criterion," *Journal of Materials Research*, vol. 29, no. 5, pp. 695–707, 2014.
- [21] M. Joun, J. G. Eom, and M. C. Lee, "A new method for acquiring true stress-strain curves over a large range of strains using a tensile test and finite element method," *Mechanics of Materials*, vol. 40, no. 7, pp. 586–593, 2008.
- [22] M. Joun, I. Choi, J. Eom, and M. Lee, "Finite element analysis of tensile testing with emphasis on necking," *Computational Materials Science*, vol. 41, no. 1, pp. 63–69, 2007.
- [23] P. W. Bridgman, *Studies in Large Plastic Flow and Fracture*, McGraw-Hill, New York, NY, USA, 1952.
- [24] J. Li, G. Yang, T. Siebert, M. F. Shi, and L. Yang, "A method of the direct measurement of the true stress-strain curve over a large strain range using multi-camera digital image correlation," *Optics and Lasers in Engineering*, vol. 107, pp. 194–201, 2018.
- [25] S. K. Paul, S. Roy, S. Sivaprasad, and S. Tarafder, "A simplified procedure to determine post-necking true stress-strain curve from uniaxial tensile test of round metallic specimen using DIC," *Journal of Materials Engineering and Performance*, vol. 27, no. 9, pp. 4893–4899, 2018.
- [26] F. Zhu, P. Bai, J. Zhang, D. Lei, and X. He, "Measurement of true stress-strain curves and evolution of plastic zone of low carbon steel under uniaxial tension using digital image correlation," *Optics and Lasers in Engineering*, vol. 65, pp. 81–88, 2015.
- [27] S. Coppieters, S. Cooreman, H. Sol, P. Van Houtte, and D. Debruyne, "Identification of the post-necking hardening behaviour of sheet metal by comparison of the internal and external work in the necking zone," *Journal of Materials Processing Technology*, vol. 211, no. 3, pp. 545–552, 2011.
- [28] GB/T 228.1-2010, *Metallic Materials-Tensile Testing-Part 1: Method of Test at Room Temperature*, China Standards Press, Beijing, China, 2010.
- [29] L. Gardner and X. Yun, "Description of stress-strain curves for cold-formed steels," *Construction and Building Materials*, vol. 189, pp. 527–538, 2018.

